Minigap-induced negative differential resistance in multilayer MoS_2-based tunnel junctions

Seiya Kawasaki,[1] Kei Kinoshita,[1] Rai Moriya,[1,*] Momoko Onodera,[1] Yijin Zhang,[1] Kenji Watanabe,[2] Takashi Taniguchi,[3] Takao Sasagawa,[4] and Tomoki Machida[1,†]

[1]*Institute of Industrial Science, University of Tokyo, 4-6-1 Komaba, Meguro, Tokyo 153-8505, Japan*
[2]*Research Center for Electronic and Optical Materials, National Institute for Materials Science, 1-1 Namiki, Tsukuba 305-0044, Japan*
[3]*Research Center for Materials Nanoarchitectonics, National Institute for Materials Science, 1-1 Namiki, Tsukuba 305-0044, Japan*
[4]*Laboratory for Materials and Structures, Tokyo Institute of Technology, 4259 Nagatsuta, Yokohama, Kanagawa 226-8503, Japan*

(Received 16 January 2024; accepted 23 May 2024; published 1 July 2024)

Despite extensive research, the high-energy band properties of transition metal dichalcogenides remain unexplored. Here, we reveal that a multilayer MoS_2-based tunnel junction exhibits substantial negative differential resistance (NDR) owing to the presence of a minigap, which is the energy gap between the upper and lower bands of the valence band at the Γ point. We fabricated a highly *p*-doped multilayer p^+-MoS_2/*h*-BN/p^+-MoS_2 tunnel junction. When a bias is applied across the junction, holes at the Fermi level at the Γ point in the valence band of the source-side p^+-MoS_2 resonantly tunnel to the drain-side p^+-MoS_2 with momentum conservation. When the energy of the injected hole coincides with the minigap of the drain-side p^+-MoS_2, the tunneling conductance is suppressed; thus, NDR is observed in the current-voltage characteristics. We identified minigap-induced NDR over a broad range of MoS_2 thicknesses, including the bulk, that was observable even at room temperature.

DOI: 10.1103/PhysRevResearch.6.033011

I. INTRODUCTION

Negative differential resistance (NDR) devices based on van der Waals (vdW) heterostructures of two-dimensional (2D) materials are becoming increasingly important because such heterostructures enable the utilization of a wide variety of 2D materials without being restricted by lattice mismatches at the interfaces [1]. As NDR devices play a crucial role in high-frequency electronics for upcoming wireless communication systems [2,3], it is imperative to develop high-performance NDR devices utilizing vdW heterostructures. This creates new opportunities for practical applications. To date, NDR in 2D materials has been demonstrated in various ways, such as via resonant tunneling through discrete energy levels [4–15] and in Esaki tunnel diodes [16–20]. Most of these previous studies have suggested that the use of vertical junctions constructed from monolayer to few-layer-thick 2D materials is crucial for the demonstration of NDR. This places severe limitations on device fabrication because (1) the thickness of the 2D material needs to be controlled with monolayer precision [21], (2) the twist angle between the source and drain layers needs to be aligned to within a few degrees to achieve matching of the in-plane momentum between the layers [22], and (3) in Esaki tunnel diodes, the carrier density of the 2D material needs to be precisely controlled to realize broken-gap type III band alignment at the heterointerface. Furthermore, 2D-material-based Esaki diodes have only been achieved using air-sensitive materials, thus device fabrication in inert environments is required [18,20,23]. Thus different approaches to realize NDR without these restrictions are required. In this study, we demonstrate that a tunnel junction fabricated without using monolayer materials, twist angle control, or broken-gap band alignment, using a highly hole-doped multilayer (ML) MoS_2 (ML p^+-MoS_2) electrode, exhibits NDR.

II. RESULTS

First, we discuss the band structure of monolayer-to-multilayer 2H-MoS_2, as shown in Fig. 1(a). The band structure was calculated using density functional theory (DFT) using a calculation method presented in our previous report [10]. The origin of the band energy ($E = 0$) was set at the top of the valence band (VB). While one-layer (1L) MoS_2 features a direct band gap at the *K* point, multilayer MoS_2 exhibits an indirect band gap between the conduction band (CB) at the *Q* point (the point between the Γ and *K* points) and the valence band (VB) at the Γ point. In addition to these band-gap changes, the structure of the VB includes other interesting features. First, the VB of MoS_2 contains upper and lower bands [blue and orange solid lines, respectively, in Fig. 1(a)], and the number of upper bands at the Γ point in the VB changes with the number of MoS_2 layers. These subbands arise owing to the out-of-plane quantum confinement in few-layer-thick MoS_2; the number of subbands in the VB at the Γ point corresponds to the number of layers *N* [24–28]. Second, the band structure of bulk MoS_2 exhibits

*Contact author: moriyar@iis.u-tokyo.ac.jp
†Contact author: tmachida@iis.u-tokyo.ac.jp

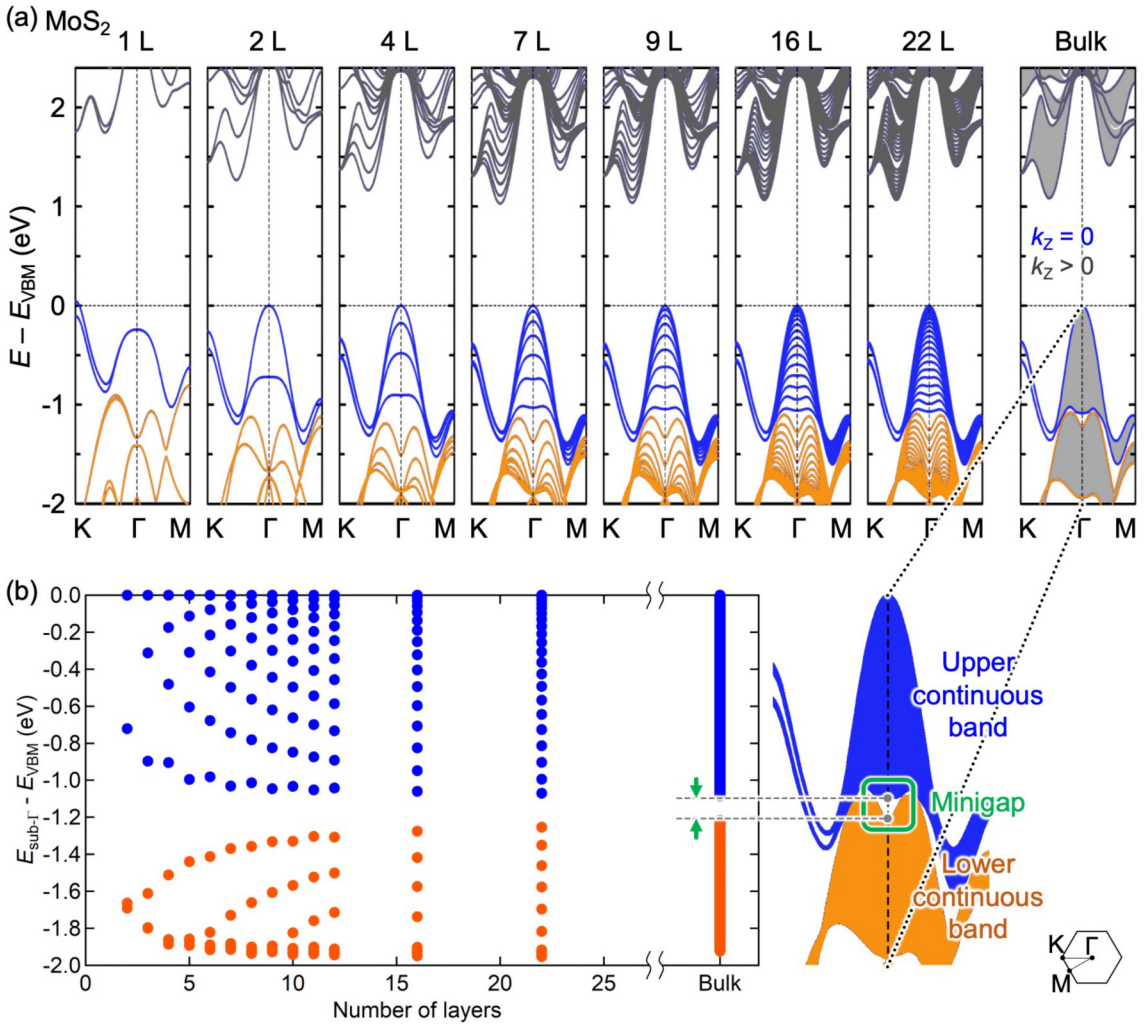

FIG. 1. (a) DFT-calculated band structures of MoS_2 for different numbers of layers N from $N = 1$ to the bulk. For each N, $E = 0$ was set at the top of VB (valence band maximum, VBM). For the band structure of the bulk (right-most plot), the bands with out-of-plane components ($k_z > 0$) are projected onto the K-Γ-M plane as gray-colored bands. (b) Left: Positions of the band energies at the Γ point ($k = 0$) in the valence band (VB) for different N (2 L to bulk). Right: Schematic illustration of the VB of bulk MoS_2 showing upper continuous band, lower continuous band, and minigap.

an energy gap between the upper and lower bands of the VB at the Γ point. In the bulk MoS_2 (right-most plot), the bands with out-of-plane components ($k_z > 0$) are projected onto the K-Γ-M plane as gray-colored bands. There is an energy gap between the upper and lower bands of the VB at the Γ point, which has the form of a characteristic down-pointing triangle (see the bottom-right panel of Fig. 1). Because this energy gap is smaller than the band gap of MoS_2, we refer to it as a minigap. The band energies at the Γ point in the VB are plotted with respect to N in Fig. 1(b); for multilayer MoS_2 (2–22 L), the energies of the subbands are plotted. For bulk MoS_2, the continuous upper and lower bands are represented by solid lines. These calculation results suggest that the minigap exists for all values of N and the center of the minigap is located −1.2 eV below the top of VB at the Γ point. The size of the minigap is approximately 0.13 eV in the bulk MoS_2. This is in stark contrast to the subband structure at the Γ point in the VB: the number of subbands and their energy levels (thus, the center between the levels) are strongly dependent on N. We note that a similar down-pointing-triangle minigap was observed in previous angle-resolved photoemission spectroscopy (ARPES) studies of bulk MoS_2 [29,30], however, thus far, no serious attempt has been made to investigate the properties of the gap. In this study, we used momentum-conserved resonant tunneling to access the minigap through transport measurements.

We fabricated a tunneling junction device with a highly p-doped multilayer p^+-MoS_2/few-layer h-BN/p^+-MoS_2 structure, where p^+-MoS_2 was the electrode and few-layer h-BN was the tunnel barrier, as illustrated in Fig. 2(a). We used Nb-doped p^+-MoS_2 with a hole density of $\sim 3 \times 10^{20}$ cm^{-3} [10,31]. Different devices using different numbers of p^+-MoS_2 layers ranging 6–50 were fabricated. Four to eight layers of h-BN were used as the tunnel barrier. During fabrication, we did not intentionally align the crystallographic orientation between the p^+-MoS_2 layers, thus it was assumed that these layers were misaligned. Further details on the device fabrication procedure are presented in Appendix A. The current-voltage (I-V_{sd}) characteristics of the junction were measured at $T = 300$ K under the application of a bias

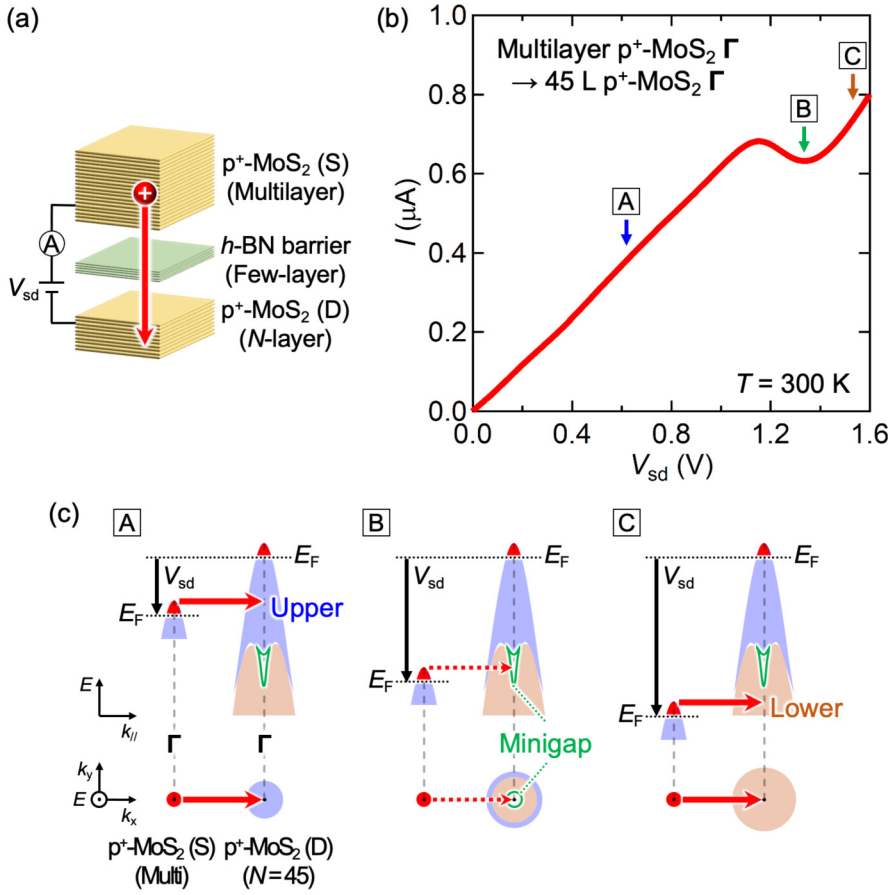

FIG. 2. (a) Schematic illustration of the device structure for highly p-doped multilayer (ML) p^+-MoS_2/few-layer h-BN/ML p^+-MoS_2 vdW tunnel junction. (b) Current-voltage (I-V_{sd}) characteristics of the device measured at $T = 300$ K. (c) Schematic illustration of resonant tunneling between hole-doped ML p^+-MoS_2 electrodes. Hole tunneling from the source-side p^+-MoS_2 [p^+-MoS_2 (S)] to the drain-side MoS_2 [p^+-MoS_2 (D)] is illustrated. Three different conditions (A, B, and C) of interlayer bias V_{sd} between p^+-MoS_2 (S) and p^+-MoS_2 (D) are considered.

V_{sd} between the p^+-MoS_2 layers, with the measurement of the current I through the device; positive V_{sd} was defined as hole tunneling from the source-side p^+-MoS_2, p^+-MoS_2 (S), to the drain-side p^+-MoS_2, p^+-MoS_2 (D). The results for the device in which the p^+-MoS_2 (S) and p^+-MoS_2 (D) layer numbers are 22 and 45 L, respectively, are shown in Fig. 2(b) (see Appendix B for the detailed device structure). The I-V_{sd} characteristics features a peak, dip, and negative differential resistance (NDR), suggesting the occurrence of resonant tunneling. We attribute positions A, B, and C in the I-V_{sd} curve [Fig. 2(b)] to the resonant tunneling of holes illustrated in panels A, B, and C, respectively, in Fig. 2(c). Since the Fermi energy E_F of p^+-MoS_2 was estimated to be ∼30 meV below the top of the VB at the Γ point (see Appendix C for details of the determination of the E_F of p^+-MoS_2), the holes in MoS_2 (S) have momentum only in the vicinity of the Γ point of p^+-MoS_2 (S), contributing to energy- and momentum-conserved tunneling. Therefore, in the following analysis, we only consider tunneling between the Γ point bands of p^+-MoS_2 (S) and p^+-MoS_2 (D). As the relative energy between p^+-MoS_2 (S) and p^+-MoS_2 (D) changes with V_{sd}, conditions A, B, and C occur. Conditions A and C correspond to resonant tunneling into the upper and lower bands of p^+-MoS_2 (D), respectively, and the tunneling conductance is high in these cases. In contrast, under condition B, the tunneling conductance was suppressed because there were no available states at the Γ point within the minigap. Thus, the I-V_{sd} curve exhibited a dip at this position. The dip is located at $V_{sd} \approx 1.3$ V; this value is close to the energy separation between the top of the VB at the Γ point and the minigap [1.2 V below the top of the VB at the Γ point, as shown in Fig. 1(a)]. Therefore, these results suggest that minigap-induced NDR can be detected from energy- and momentum-conserved resonant tunneling.

We believe that the momentum-conserved resonant hole tunneling between the Γ points of p^+-MoS_2 (S) and p^+-MoS_2 (D) is crucial for observing minigap-induced NDR. To confirm this hypothesis, we fabricated a reference device: monolayer WSe_2/few-layer h-BN/38L p^+-MoS_2 (see Appendix D, for details of the device structure). The difference between this device and the device shown in Fig. 2 is that monolayer WSe_2, in which the Fermi energy is located in the VB at the K point, was used as the source electrode instead of p^+-MoS_2 (S). We then consider hole tunneling from the source-side hole-doped monolayer WSe_2, p-WSe_2 (S), to p^+-MoS_2 (D), as illustrated in Fig. 3(a). Because the Fermi energy of monolayer p-WSe_2 is close to the top of the VB at the K point, momentum-conserved tunneling between the Γ points of the VBs is prohibited, as illustrated by the dashed arrow in the figure. Indeed, the I-V_{sd} curve measured for the device [Fig. 3(b)] does not show apparent NDR at $T = 300$ K within the measured V_{sd} range. The small inflection in the I-V_{sd} curve near $V_{sd} = +1.2$ V is attributable to tunneling from the VB at the K point in p-WSe_2 (S) to the VB at the Γ point of p^+-MoS_2 (D); however, this is not momentum-conserved tunneling, and thus does not show NDR. This finding is fur-

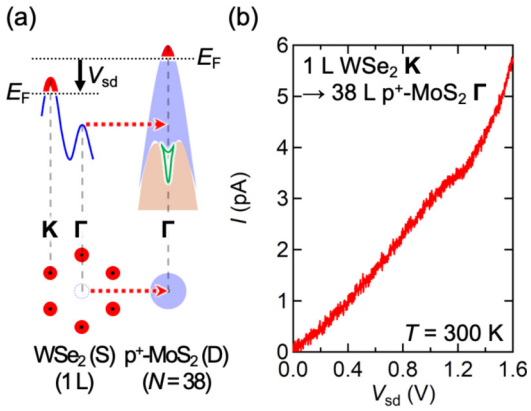

FIG. 3. (a) Schematic illustration of tunneling process from a hole-doped monolayer WSe_2 to ML MoS_2. The crystallographic orientations of the monolayer WSe_2 and p^+-MoS_2 layers were such that they were considered to be misaligned. (b) I-V_{sd} characteristics of the device measured at $T = 300$ K.

ther evidence of the cruciality of using momentum-conserved hole tunneling between the Γ points of the VBs to observe minigap-induced NDR, as shown in Fig. 2.

We now address the impact of the number of layers N of MoS_2 (D) on the NDR. We fabricated p^+-MoS_2 (S)/few-layer h-BN/p^+-MoS_2 (D) with different N values from 45 to 6 L, and the I-V_{sd} curves were measured at different temperatures from 20 to 300 K; these are compared in Fig. 4(a) (see Appendix E for details of the device structures of the different devices). The $N = 45$ L device (the same device is shown in Fig. 2), the data for which are featured at the top of Fig. 4(a), exhibits minigap-induced NDR, as highlighted by the green shaded area, that is nearly temperature-independent. For smaller N values of 16, 9, and 6, the I-V_{sd} curves exhibit different behaviors. Specifically, the curves exhibit oscillatory behavior, showing NDR as highlighted by the blue shaded areas. The peaks of the oscillation are marked by blue squares, circles, triangles, diamonds, and pentagons. The position of the oscillation peaks changed with N, and the amplitude of

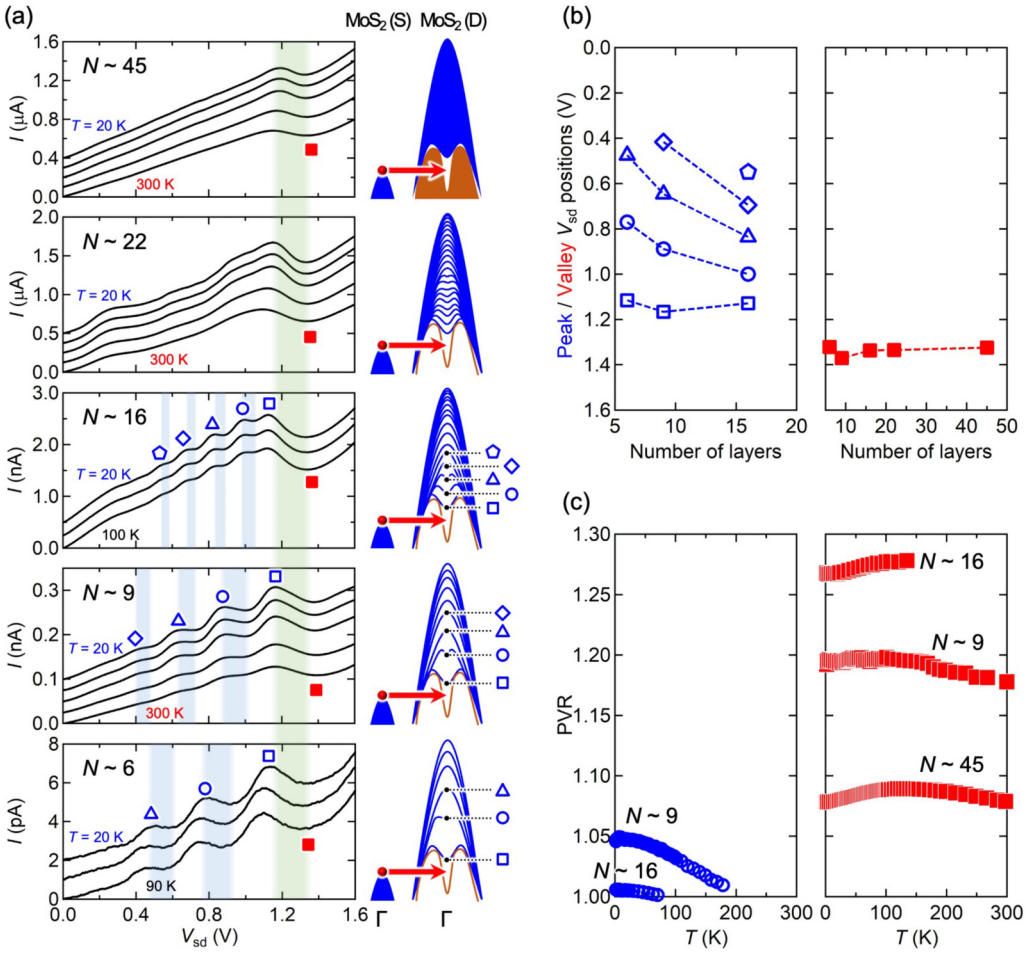

FIG. 4. (a) Left: I-V_{sd} characteristics for ML p^+-MoS_2/few-layer h-BN/ML p^+-MoS_2 tunnel junction with different N for drain-side MoS_2. The I-V_{sd} curves for different temperatures ($T = 20$, 60, 100, 200, and 300 K for $N = 45$, 22, and 9. $T = 20$, 60, and 100 K for $N = 16$. $T = 20$, 60, and 90 K for $N = 6$) are plotted. The peaks in the I-V_{sd} curve are highlighted by blue squares, circles, triangles, diamonds, and pentagons. Right: illustrations of VB structures of MoS_2 (S) and MoS_2 (D). (b) Left: V_{sd} positions of resonant tunneling peaks in the I-V_{sd} curves shown in panel (a). Right: V_{sd} positions of the dips in the I-V_{sd} curves marked by red solid squares in panel (a). The V_{sd} positions were obtained from the data at $T = 20$ K except for $N = 6$, which was obtained from the data at $T = 60$ K. (c) Temperature dependence of PVR for (left) subband-induced NDR and (right) minigap-induced NDR.

oscillation decreased at higher temperatures (this is especially apparent in the data for $N = 9$); thus, these oscillations are both N and temperature dependent. We recently observed similar oscillatory behavior as well as temperature-dependent behavior in a multilayer p^+-MoS_2/h-BN/few-layer WSe_2 [10] and few-layer WSe_2/h-BN/few-layer WSe_2 junction [11]. Therefore, we assigned these peaks to resonant tunneling into the quantized subbands of the VB at the Γ point, as illustrated schematically on the right side of Fig. 4(a). Because the energy spacing between the subbands changes with N, the peak position of the resonant tunneling also changes with N. In contrast to the N-dependent behavior of the subband-induced resonant tunneling, we found that minigap-induced NDR was independent of N and temperature. For example, the position of the dip assigned to minigap-induced NDR, marked by the red solid square, is nearly identical for the junctions with different N, and NDR is clearly seen even at 300 K. Therefore, minigap-induced NDR was found to be robust against N and temperature changes. In addition to these features, we observed that the I-V_{sd} curves exhibited other peaks that could be assigned to tunneling into the impurity band of Nb, as discussed in Appendix F.

The V_{sd} positions of the peaks and dips were plotted versus N in Fig. 4(b). This plot further confirms that the peaks arising from resonant tunneling into subbands depend on N (left panel), and the position of the dip due to minigap-induced NDR does not depend on N (right panel). In addition, in Fig. 4(c), the peak-to-valley ratio (PVR) of the NDR (peak I/dip I) is plotted versus temperature for the subband-induced NDR (left) and minigap-induced NDR (right). The temperature dependence is substantially different for the minigap- and subband-induced NDRs. While the PVR of the subband-induced NDR decreased with increasing temperature and disappeared (was <1) at 300 K, the PVR of the minigap-induced NDR remained the same across the entire temperature range. This difference can be attributed to the band structure of MoS_2 [Fig. 1(a)]. DFT calculations suggest that the separation between the subbands at the Γ point in the VB decreases with N and goes to zero at the bulk limit. This is in stark contrast to the minigap, which exists for all values of N and in the bulk material (additional data sets for the detailed N dependence of minigap-induced NDR features are presented in Appendix G).

Taken together, the results discussed above reveal the unique properties of minigap-induced NDR, which include the following: (1) a wide range of thicknesses of multilayer MoS_2 can be used to demonstrate NDR because it is insensitive to the thickness of MoS_2, (2) resonant tunneling between the VBs at the Γ points does not require alignment of the crystallographic orientations of MoS_2 (S) and MoS_2 (D) [11], and (3) as long as both p^+-MoS_2 (S) and p^+-MoS_2 (D) are conductive, there are no serious restrictions on the doping level of the p^+-MoS_2 layers. We believe that these are significant advantages for constructing high-frequency electronic devices based on multilayer p^+-MoS_2.

III. SUMMARY

We investigated the tunneling transport in a highly p-doped multilayer (ML) p^+-MoS_2/few-layer h-BN/ML p^+-MoS_2 vdW junction. The results showed that in the presence of energy- and momentum-conserved tunneling, the gap between the upper and lower bands within the VB of MoS_2 gives rise to negative differential resistance at 300 K. We showed that the minigap-induced NDR is robust to changes in the MoS_2 thickness and temperature under our experimental conditions. Because this phenomenon was observed even when we used almost bulklike thick multilayer MoS_2, our results provide a direction for the development of electronics applications utilizing multilayer transition metal dichalcogenides (TMDs).

ACKNOWLEDGMENTS

This work was supported by JST-CREST, JST-Mirai, and JST-PRESTO (Grants No. JPMJCR15F3, No. JPMJCR20B4, No. JPMJMI21G9, and No. JPMJPR20L5); JSPS KAKENHI (Grants No. JP20H00127, No. JP20H00354, No. JP21H04652, No. JP21H05232, No. JP21H05233, No. JP21H05234, No. JP21H05236, No. JP21K18181, No. JP22H01898, No. JP22K18317, No. JP22K14559, No. JP22J22105, No. JP22KJ1104, and No. JP23H02052); the Kenjiro Takayanagi Foundation; the Inoue Foundation for Science; Tokuyama Science Foundation; and Support Center for Advanced Telecommunications Technology Research Foundation.

APPENDIX A: DEVICE FABRICATION AND MEASUREMENT METHODS

Bulk crystals of both Nb-doped p-type MoS_2 (p^+-MoS_2) and nondoped WSe_2 were purchased from HQ Graphene Inc. High-quality h-BN bulk crystals were grown using a high-pressure, high-temperature method. First, thin crystals of p^+-MoS_2, WSe_2, and h-BN were exfoliated from the bulk crystal and deposited on an 85- or 290-nm SiO_2/Si substrate. The exfoliation procedure was reported in our previous publication [11]. The thicknesses of the flakes were determined by means of optical contrast and atomic force microscopy (AFM) measurements.

vdW heterostructure devices were fabricated via a polymer-based van der Waals (vdW) pick-up method using poly(bisphenol A carbonate) (PC) on a PDMS sheet as the polymer material. The fabrication procedure for the p^+-MoS_2/few-layer h-BN/p^+-MoS_2 device was as follows. First, the top h-BN layer (with a thickness of 30–60 nm) was picked up with the PC on PDMS. Using this h-BN, the top p^+-MoS_2 (42–45 layers), tunnel barrier h-BN (4–8 layers), bottom p^+-MoS_2 (6–22 layers), and bottom h-BN (30–60 nm thick) were sequentially picked up. Finally, the heterostructure on the PC was transferred onto a 290-nm-thick SiO_2/p-doped

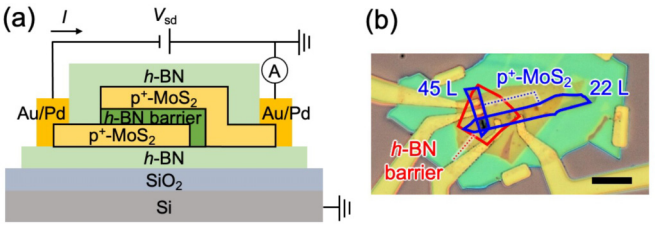

FIG. 5. (a) Schematic illustration of the 45L p^+-MoS_2/4–5L h-BN/22L p^+-MoS_2 device structure. (b) Optical micrograph of the fabricated device.

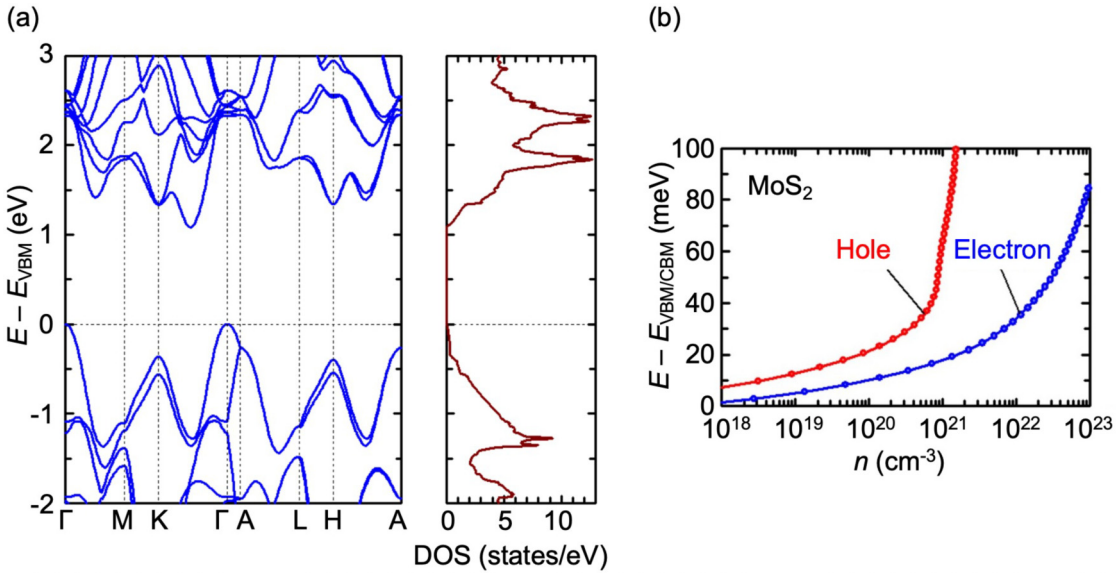

FIG. 6. (a) Band structure of bulk MoS_2 calculated using DFT. (b) Fermi energies of electrons and holes as a function of carrier density n.

Si substrate. During the flake pickup and the transfer of the heterostructure onto the SiO_2/Si substrate, temperature was maintained at 130 and 180 °C, respectively.

To fabricate the WSe_2/few-layer h-BN/p^+-MoS_2 device, after the top h-BN layer, monolayer WSe_2, tunnel barrier h-BN, and bottom p^+-MoS_2 layers had been picked up, another p^+-MoS_2 was picked up, and this was used to construct an Ohmic contact with WSe_2 [31]. Finally, the bottom h-BN was picked up, and the heterostructure was transferred onto a 290-nm-thick SiO_2/p-doped Si substrate.

To fabricate an electrical contact with the device, electrode patterns were prepared by electron beam (EB) lithography using poly(methyl methacrylate) (PMMA) as a resist. After fabricating the PMMA pattern for the electrodes, reactive ion etching (RIE) (Samco, RIE200iP) with CF_4 gas was performed to remove a part of the top h-BN and p^+-MoS_2 layers. After RIE, the sample was loaded into an EB evaporator and a metal stack of Au (80 nm)/Pd (20 nm) was deposited to form Ohmic contacts with the p^+-MoS_2. Owing to the high Nb doping of p^+-MoS_2, an Ohmic contact between Au/Pd and p^+-MoS_2 was obtained [31].

To fabricate the top-gate electrode, PMMA patterns were first fabricated by EB lithography, and an Au (90 nm)/Cr (5 nm) stack was deposited using an EB evaporator.

Transport properties were measured using a variable-temperature cryostat. The current-voltage (I-V_{int}) characteristics were measured by applying a source-drain bias V_{int} and the current flowing through the device was measured using a current amplifier (DL instruments, Model 1211). V_{int} and the top-gate voltage V_G were applied using a Keithley 2400 source measurement unit.

APPENDIX B: DETAILED STRUCTURE OF p^+-MoS_2/h-BN/p^+-MoS_2 DEVICE PRESENTED IN FIG. 2

The detailed device structure of the p^+-MoS_2/h-BN/p^+-MoS_2 device presented in Fig. 2 is shown in Fig. 5.

APPENDIX C: DETERMINATION OF THE FERMI ENERGY OF p^+-MoS_2

The band structure, density of states (DOS), and Fermi energy calculated using DFT are shown in Fig. 6.

APPENDIX D: DETAILED STRUCTURE OF WSe_2/h-BN/p^+-MoS_2 DEVICE PRESENTED IN FIG. 3

The detailed device structure of the monolayer WSe_2/h-BN/p^+-MoS_2 device presented in Fig. 3 is shown in Fig. 7.

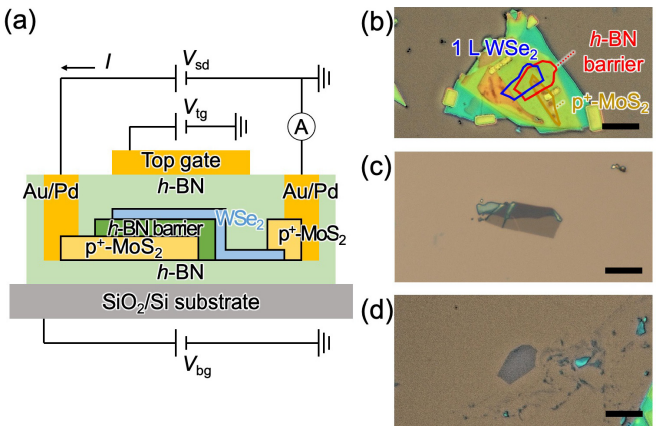

FIG. 7. (a) Schematic illustration of the monolayer WSe_2/few-layer h-BN/38L p^+-MoS_2 device structure. A top gate voltage V_{tg} of −10.5 V was applied to the top h-BN dielectric with a thickness of 34 nm to hole-dope the WSe_2 monolayer during the transport measurement. (b) An optical micrograph of the fabricated device. (c) An optical micrograph of the monolayer WSe_2 on the 290-nm SiO_2/Si substrate. (d) An optical micrograph of the thin h-BN flake on the 290-nm SiO_2/Si. Scale bars: 10 μm.

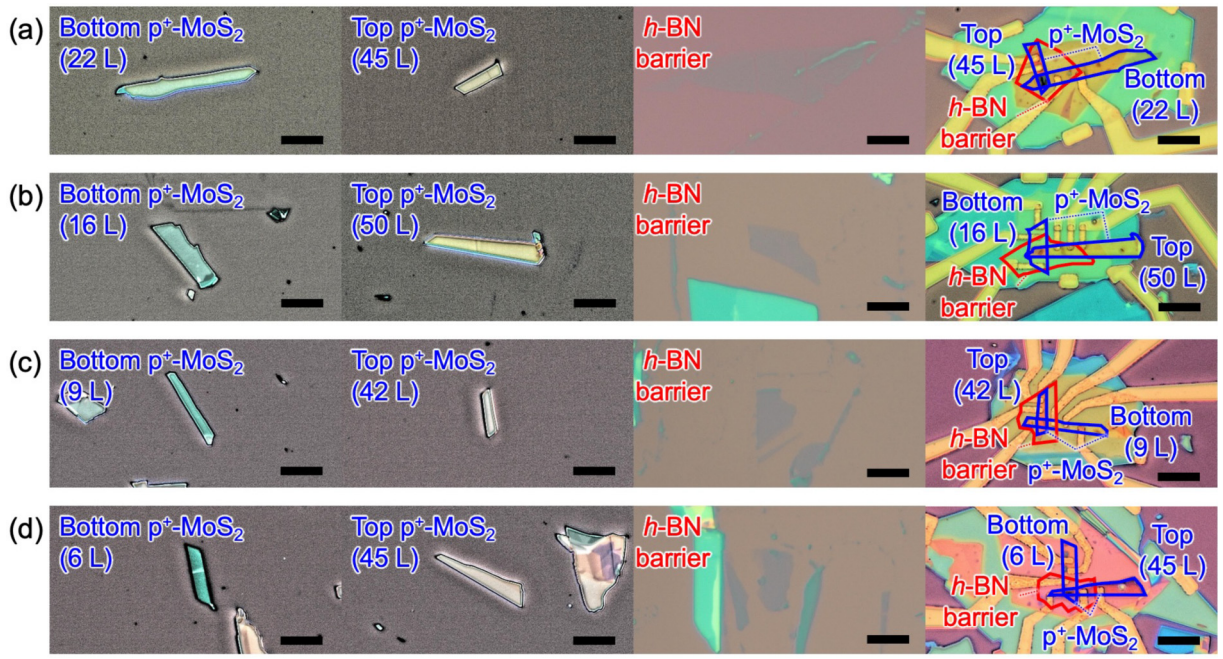

FIG. 8. (a)–(d) Left: optical micrographs of p^+-MoS_2 lakes on 290-nm SiO_2/Si substrate used in the devices. Middle: optical micrographs of h-BN lakes on 290-nm SiO_2/Si substrate used in the devices. Right: optical micrographs of fabricated devices. Scale bars: 10 μm.

APPENDIX E: OPTICAL MICROGRAPHS OF ALL THE DEVICES AND p^+-MoS_2 FLAKES EXAMINED IN THIS STUDY

Optical micrographs of the devices, exfoliated p^+-MoS_2 flakes, and exfoliated h-BN flakes used in this study are summarized in Fig. 8.

APPENDIX F: TUNNELING FEATURES RELATED TO THE Nb IMPURITY BAND IN MoS_2

The I-V_{sd} curves for $N = 22$, 16, and 9, shown in Fig. 9(a), exhibit additional peaks indicated by filled

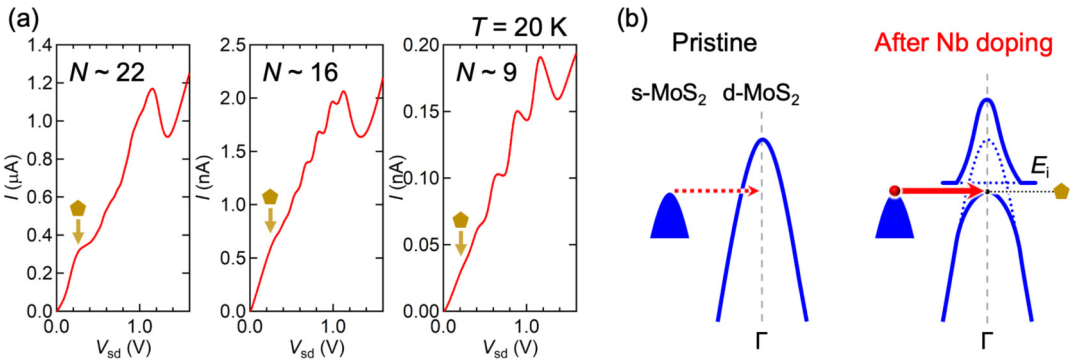

FIG. 9. (a) I-V_{sd} curves for $N = 22$, 16, and 9 measured at 20 K. (b) Schematic illustration of tunneling into Nb impurity band.

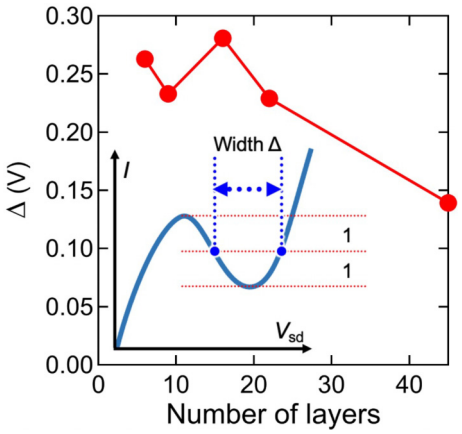

FIG. 10. The width of the dip Δ in the I-V_{sd} curve is plotted for different N.

dark-yellow hexagons. This can be attributed to the Nb impurity band formed in highly Nb-doped p^+-MoS_2, as schematically illustrated in Fig. 9(b). The presence of the Nb impurity band has been previously reported in Nb-doped p^+-MoS_2 crystals with similar hole densities [32].

APPENDIX G: RELATIONSHIP BETWEEN MINIGAP-INDUCED NDR AND DRAIN-SIDE p^+-MoS_2 THICKNESS

The width of the dip in the I-V_{sd} curves for minigap-induced NDR was extracted for different N values, and the results are shown in Fig. 10. The width decreases with N, as we expected from the N dependence of the minigap size shown in Fig. 1.

[1] A. Chaves, J. G. Azadani, H. Alsalman, D. R. da Costa, R. Frisenda, A. J. Chaves, S. H. Song, Y. D. Kim, D. He, J. Zhou, A. Castellanos-Gomez, F. M. Peeters, Z. Liu, C. L. Hinkle, S.-H. Oh, P. D. Ye, S. J. Koester, Y. H. Lee, P. Avouris, X. Wang, and T. Low, Bandgap engineering of two-dimensional semiconductor materials, npj 2D Mater. Appl. **4**, 29 (2020).

[2] S. Suzuki, Resonant tunneling diode technology for future terahertz applications, in *2022 International Electron Devices Meeting (IEDM), San Francisco, CA* (IEEE, Piscataway, NJ, 2022), p. 4.4.1.

[3] M. Asada and S. Suzuki, Terahertz emitter using resonant-tunneling diode and applications, Sensors **21**, 1384 (2021).

[4] L. Britnell, R. V. Gorbachev, A. K. Geim, L. A. Ponomarenko, A. Mishchenko, M. T. Greenaway, T. M. Fromhold, K. S. Novoselov, and L. Eaves, Resonant tunnelling and negative differential conductance in graphene transistors, Nat. Commun. **4**, 1794 (2013).

[5] A. Mishchenko, J. S. Tu, Y. Cao, R. V. Gorbachev, J. R. Wallbank, M. T. Greenaway, V. E. Morozov, S. V. Morozov, M. J. Zhu, S. L. Wong, F. Withers, C. R. Woods, Y. J. Kim, K. Watanabe, T. Taniguchi, E. E. Vdovin, O. Makarovsky, T. M. Fromhold, V. I. Fal'ko, A. K. Geim *et al.*, Twist-controlled resonant tunnelling in graphene/boron nitride/graphene heterostructures, Nat. Nanotechnol. **9**, 808 (2014).

[6] G. W. Burg, N. Prasad, B. Fallahazad, A. Valsaraj, K. Kim, T. Taniguchi, K. Watanabe, Q. Wang, M. J. Kim, L. F. Register, and E. Tutuc, Coherent interlayer tunneling and negative differential resistance with high current density in double bilayer Graphene–WSe_2 heterostructures, Nano Lett. **17**, 3919 (2017).

[7] S. Kang, N. Prasad, H. C. P. Movva, A. Rai, K. Kim, X. Mou, T. Taniguchi, K. Watanabe, L. F. Register, E. Tutuc, and S. K. Banerjee, Effects of electrode layer band structure on the performance of multilayer Graphene-hBN-Graphene interlayer tunnel field effect transistors, Nano Lett. **16**, 4975 (2016).

[8] B. Fallahazad, K. Lee, S. Kang, J. Xue, S. Larentis, C. Corbet, K. Kim, H. C. P. Movva, T. Taniguchi, K. Watanabe, L. F. Register, S. K. Banerjee, and E. Tutuc, Gate-Tunable resonant tunneling in double bilayer graphene heterostructures, Nano Lett. **15**, 428 (2015).

[9] K. Kim, N. Prasad, H. C. P. Movva, G. W. Burg, Y. Wang, S. Larentis, T. Taniguchi, K. Watanabe, L. F. Register, and E. Tutuc, Spin-Conserving resonant tunneling in twist-controlled WSe_2-hBN-WSe_2 heterostructures, Nano Lett. **18**, 5967 (2018).

[10] K. Takeyama, R. Moriya, S. Okazaki, Y. Zhang, S. Masubuchi, K. Watanabe, T. Taniguchi, T. Sasagawa, and T. Machida, Resonant tunneling due to van der waals quantum-well states of few-layer WSe_2 in WSe_2/*h*-BN/p^+-MoS_2 junction, Nano Lett. **21**, 3929 (2021).

[11] K. Kinoshita, R. Moriya, S. Okazaki, Y. Zhang, S. Masubuchi, K. Watanabe, T. Taniguchi, T. Sasagawa, and T. Machida, Resonant tunneling between quantized subbands in van der waals double quantum well structure based on few-layer WSe_2, Nano Lett. **22**, 4640 (2022).

[12] P. K. Srivastava, Y. Hassan, D. J. P. de Sousa, Y. Gebredingle, M. Joe, F. Ali, Y. Zheng, W. J. Yoo, S. Ghosh, J. T. Teherani, B. Singh, T. Low, and C. Lee, Resonant tunnelling diodes based on twisted black phosphorus homostructures, Nat. Electron. **4**, 269 (2021).

[13] K. Xu, E. Wynne, and W. Zhu, Resonant tunneling and negative differential resistance in black phosphorus vertical heterostructures, Adv. Electron. Mater. **6**, 2000318 (2020).

[14] Z. Zhang, B. Zhang, Y. Wang, M. Wang, Y. Zhang, H. Li, J. Zhang, and A. Song, Toward high-peak-to-valley-ratio graphene resonant tunneling diodes, Nano Lett. **23**, 8132 (2023).

[15] S. Zheng, S. Jo, K. Kang, L. Sun, M. Zhao, K. Watanabe, T. Taniguchi, P. Moon, N. Myoung, and H. Yang, Resonant tunneling spectroscopy to probe the giant stark effect in atomically thin materials, Adv. Mater. **32**, 1906942 (2020).

[16] T. Roy, M. Tosun, X. Cao, H. Fang, D.-H. Lien, P. Zhao, Y.-Z. Chen, Y.-L. Chueh, J. Guo, and A. Javey, Dual-Gated MoS_2/WSe_2 van der waals tunnel diodes and transistors, ACS Nano **9**, 2071 (2015).

[17] P. Paletti, R. Yue, C. Hinkle, S. K. Fullerton-Shirey, and A. Seabaugh, Two-dimensional electric-double-layer Esaki diode, npj 2D Mater. Appl. **3**, 19 (2019).

[18] R. Yan, S. Fathipour, Y. Han, B. Song, S. Xiao, M. Li, N. Ma, V. Protasenko, D. A. Muller, D. Jena, and H. G. Xing, Esaki Diodes in van der Waals heterojunctions with broken-gap energy band alignment, Nano Lett. **15**, 5791 (2015).

[19] Y.-C. Lin, R. K. Ghosh, R. Addou, N. Lu, S. M. Eichfeld, H. Zhu, M.-Y. Li, X. Peng, M. J. Kim, L.-J. Li, R. M. Wallace, S. Datta, and J. A. Robinson, Atomically thin resonant tunnel diodes built from synthetic van der Waals heterostructures, Nat. Commun. **6**, 7311 (2015).

[20] N. Abraham, K. Murali, K. Watanabe, T. Taniguchi, and K. Majumdar, Astability versus bistability in van der Waals tunnel diode for voltage controlled oscillator and memory applications, ACS Nano **14**, 15678 (2020).

[21] S. Masubuchi, M. Morimoto, S. Morikawa, M. Onodera, Y. Asakawa, K. Watanabe, T. Taniguchi, and T. Machida, Autonomous robotic searching and assembly of two-dimensional crystals to build van der Waals superlattices, Nat. Commun. **9**, 1413 (2018).

[22] K. Kim, M. Yankowitz, B. Fallahazad, S. Kang, H. C. P. Movva, S. Huang, S. Larentis, C. M. Corbet, T. Taniguchi, K. Watanabe, S. K. Banerjee, B. J. LeRoy, and E. Tutuc, van der Waals heterostructures with high accuracy rotational alignment, Nano Lett. **16**, 1989 (2016).

[23] S. Fan, Q. A. Vu, S. Lee, T. L. Phan, G. Han, Y.-M. Kim, W. J. Yu, and Y. H. Lee, Tunable negative differential resistance in van der Waals heterostructures at room temperature by tailoring the interface, ACS Nano **13**, 8193 (2019).

[24] P. Schmidt, F. Vialla, S. Latini, M. Massicotte, K.-J. Tielrooij, S. Mastel, G. Navickaite, M. Danovich, D. A. Ruiz-Tijerina, C. Yelgel, V. Fal'ko, K. S. Thygesen, R. Hillenbrand, and F. H. L. Koppens, Nano-imaging of intersubband transitions in van der Waals quantum wells, Nat. Nanotechnol. **13**, 1035 (2018).

[25] D. A. Ruiz-Tijerina, M. Danovich, C. Yelgel, V. Zólyomi, and V. I. Fal'ko, Hybrid k·p tight-binding model for subbands and infrared intersubband optics in few-layer films of transition-metal dichalcogenides: MoS_2, $MoSe_2$, WS_2, and WSe_2, Phys. Rev. B **98**, 035411 (2018).

[26] Y. Wang, L. Wu, Z. Wei, Z. Liu, P. Cheng, Y. Zhang, B. Feng, G. Zhang, W. Ji, K. Wu, and L. Chen, Real-space detection and manipulation of two-dimensional quantum well states in few-layer MoS_2, Phys. Rev. B **105**, L081404 (2022).

[27] A. Kuc, N. Zibouche, and T. Heine, Influence of quantum confinement on the electronic structure of the transition metal sulfide TS_2, Phys. Rev. B **83**, 245213 (2011).

[28] W. Jin, P.-C. Yeh, N. Zaki, D. Zhang, J. T. Sadowski, A. Al-Mahboob, A. M. van der Zande, D. A. Chenet, J. I. Dadap, I. P. Herman, P. Sutter, J. Hone, and R. M. Osgood, Direct measurement of the thickness-dependent electronic band structure of MoS_2 using angle-resolved photoemission spectroscopy, Phys. Rev. Lett. **111**, 106801 (2013).

[29] H. Coy Diaz, J. Avila, C. Chen, R. Addou, M. C. Asensio, and M. Batzill, Direct observation of interlayer hybridization and dirac relativistic carriers in Graphene/MoS_2 van der Waals heterostructures, Nano Lett. **15**, 1135 (2015).

[30] A. Kar, S. K. Mahatha, and K. S. R. Menon, Polarization-dependent electronic structure of Ag quantum well states on the MoS_2(0001) surface using ARPES and DFT studies, Phys. Rev. B **106**, 235146 (2022).

[31] K. Takeyama, R. Moriya, K. Watanabe, S. Masubuchi, T. Taniguchi, and T. Machida, Low-temperature p-type ohmic contact to WSe_2 using p^+-MoS_2/WSe_2 van der Waals interface, Appl. Phys. Lett. **117**, 153101 (2020).

[32] J. Suh, T. L. Tan, W. Zhao, J. Park, D.-Y. Lin, T.-E. Park, J. Kim, C. Jin, N. Saigal, S. Ghosh, Z. M. Wong, Y. Chen, F. Wang, W. Walukiewicz, G. Eda, and J. Wu, Reconfiguring crystal and electronic structures of MoS_2 by substitutional doping, Nat. Commun. **9**, 199 (2018).